Stress Relaxation for Granular Materials near Jamming under Cyclic Compression

Somayeh Farhadi, Alex Z. Zhu, and Robert P. Behringer
Department of Physics and Center for Nonlinear and Complex Systems, Box 90305, Duke University, Durham, North Carolina 27708, USA

(Received 26 September 2013; revised manuscript received 27 May 2014; published 29 October 2015)

We have explored isotropically jammed states of semi-2D granular materials through cyclic compression. In each compression cycle, systems of either identical ellipses or bidisperse disks transition between jammed and unjammed states. We determine the evolution of the average pressure P and structure through consecutive jammed states. We observe a transition point ϕ_m above which P persists over many cycles; below ϕ_m, P relaxes slowly. The relaxation time scale associated with P increases with packing fraction, while the relaxation time scale for collective particle motion remains constant. The collective motion of the ellipses is hindered compared to disks because of the rotational constraints on elliptical particles.

DOI: 10.1103/PhysRevLett.115.188001 PACS numbers: 45.70.-n, 61.43.-j, 62.40.+i

Introduction.—Particle systems near jamming exhibit several signature features, including dynamical slowing down and heterogeneous dynamics [1,2]. Systems of interest include colloids, molecular glass formers, and granular materials [3–6]. Although all these systems can jam, granular materials, which we consider here, have the experimental advantage of accessibility at the particle scale. We use this feature to explore the dynamics of isotropically driven disordered materials near jamming.

Although these systems all share certain common features, several aspects distinguish studies of them, including excitation mechanisms and interparticle interactions. In molecular and colloidal systems, temperature provides homogeneous driving. In granular systems, temperature is an irrelevant variable, and driving must be provided externally. In past granular studies, driving came from vibration or tapping [7–9], by biaxial strain [10], or by shear [11–14]. Much of the work on vibration and tapping has been summarized by Richard *et al.* [7] and usually involves energy input on rapid time scales in ways that may not be isotropic and uniform. Alonso-Maroquín and Herrmann [10] focused on the role of friction at contacts for biaxial cyclic strain applied to systems of irregular 2D polygons, which always existed in a jammed state (with nonzero stresses). Shear strain can be applied on any time scale, but it is anisotropic and not necessarily homogeneous; e.g., shear failures are often localized [15,16]. The first point of the present experiments is to understand the effect of jamming on granular systems when the driving mechanism is (relatively) uniform, isotropic, and on slow time scales.

Previous studies of spatiotemporal granular dynamics near jamming have typically involved spherically symmetric particles: disks in 2D and spheres in 3D. In recent experiments, we showed that tangential forces for frictional particles significantly change stable states near jamming [17] and help stabilize the granular network ("force chains"). If friction stabilizes granular networks by limiting rotation, it is natural to probe the possibly similar role played by geometry, and this is the second question that we address here. As we show below, although both types of systems slow down under cyclic driving as the density grows, the characteristic time scales for ellipses is significantly greater than for disks.

In the present experiments, we cyclically and isotropically compress or expand our granular systems by small amounts, starting from a packing fraction ϕ, just below isotropic jamming, and compressing to a ϕ that is above isotropic jamming. We measure the mean pressure P and the collective dynamics in the most compressed states for very large numbers of cycles. Under this protocol, the system may slowly find more compact configurations. The time associated with this evolution becomes large as ϕ for the compressed state grows, whereas the time scale for the evolution of inhomogeneities of particle motion remains roughly constant. We emphasize that the most compressed ϕ during a cycle is always above isotropic jamming, e.g., $\phi_c \simeq 0.84$ for disks [18] and $\phi_c \simeq 0.91$ for ellipses [19].

Experiment.—The experiments consisted of cyclic isotropic compression of quasi-2D systems of bidisperse disks and systems of identical ellipses with an aspect ratio ~2. A schematic of the setup is shown in Fig. 1. The particles were confined in a square container, a biax, where two of the confining walls were stationary, while the other two were displaced using linear motors. The distance between opposing pairs of walls has a spatial resolution of $\sim 10^{-6}$ m. The number of particles was kept constant at 2400 in all the experiments. By changing the confining area of the biax [17], we changed the packing fraction. The packing fractions ϕ of the fully compressed states were chosen to be above the isotropic jamming point (point J). Here we refer to point J as the packing fraction of a system under isotropic compression, where the coordination number Z begins to grow as a power law [19]. We have introduced

 © 2015 American Physical Society

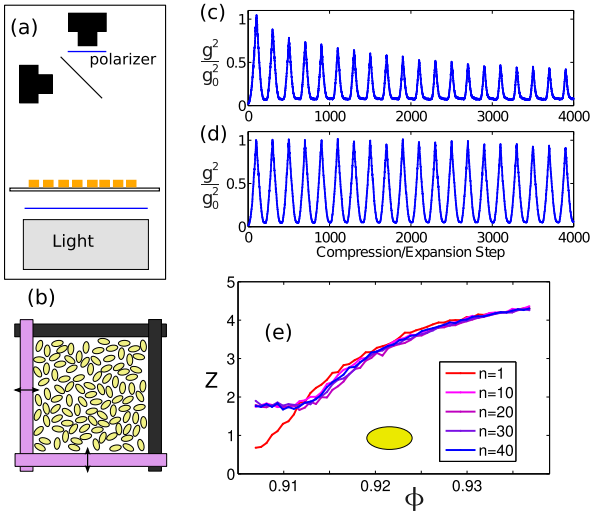

FIG. 1 (color online). Schematics of the biax. (a) Particles are confined inside a square region. (b) Side view. (c,d) Time series of global g^2 for two sets of cyclic compression of ellipses performed in different packing fraction intervals of (c) [0.868, 0.896] and (d) [0.906, 0.937]. The values of g^2 are normalized by g^2 at the most compressed state of the first cycle (g_0^2). The system is compressed by 1.6% in a series of much smaller quasistatic steps. (e) Coordination number Z vs packing fraction. All the particles (including rattlers) are counted in calculating Z. The power-law growth of Z at $\phi \simeq 0.91$ indicates the onset of isotropic jamming transition. Here, n is the compression cycle. $n = 1$ corresponds to the transient response.

point J in this study because any cyclic dynamics dies out very quickly if the system is below and far from the isotropic jamming point. The particles were photoelastic, which allowed us to measure the local pressure acting on each particle. Before starting any compression cycle, the system was prepared in a stress-free state. It was then quasistatically compressed via many small strain steps (about 0.016%) for a typical total volumetric strain of 3.2%. Next, it was quasistatically expanded to its initial strain-free state. This process was repeated for multiple cycles. Some initial runs were made for which the system was imaged at every strain step for multiple compression steps and relaxations. For longer numbers of compression cycles (up to ~1000 cycles), the system was strained as above but imaged only once at the maximum compressive strain for each cycle. Before imaging at this strain extremum, the system was allowed to relax. The imaging was carried out using two synchronized digital cameras, one of which recorded a polarized image that yielded the photoelastic response of the system, while the other recorded a normal (unpolarized) image. These two images enabled us to measure the local stress on each particle and to track the particles, including their centers and orientations (for ellipses).

The quasi-2D particles, either circular (disks) or ellipses, are machined from sheets of Vishay polymer PSM-4 that are 0.635 cm thick. The semiminor axis of the ellipses is $b \simeq 0.25$ cm, and the aspect ratio is 1.85. The system of disks is bidisperse, where the ratio of small-to-large particles is kept at about 4.5:1. The radius of small disks is $r_s \simeq 0.38$ cm, and the radius of larger particles is $r_l \simeq 0.44$ cm. The particles rest on a horizontal Plexiglas sheet [Fig. 1(a)] that has been lubricated by a layer of fine powder. As shown in Fig. 1(a), a circularly polarized beam passes through the Plexiglas sheet and the particles from below, and then through a beam splitter placed over the setup. The beam splitter provides two identical images, one of which is viewed without a polarizer by the horizontal camera, while the other passes through a crossed circular polarizer (with respect to the bottom polarizer) and is viewed by the top camera. The two cameras acquire images simultaneously. As a result, one camera records the photoelastic response of the system (polarized image), and the other camera yields a direct image (normal image) of the particles for tracking. We extracted the local stress acting on each particle, which is encoded in the photoelastic response, using an established empirical measure which we call g^2. This quantity is the gradient squared of the transmitted photoelastic image intensity integrated over the pixels associated with each particle [12]. Before computing g^2, we first filter the photoelastic images, leaving only the green channel of the original color image, which corresponds to the optimum color response of the polarizers. The global stress is found by averaging g^2 over all particles in each image at a given strain.

Global stress response.—Figures 1(c) and 1(d) show time series of the global stress of the ellipses for two packing fraction intervals (i.e., minimum and maximum ϕ's), which are obtained by incrementally compressing or expanding the system over a number of cycles. In Figs. 1(c) and 1(d), the global values of g^2 are normalized by the global g^2 at the most compressed state of the first cycle (g_0^2), which always corresponds to a density that is above the isotropic jamming point. For the lower packing fraction, Fig. 1(c), we see a gradual drop of the maximum global g^2. Although the system is effectively "jammed" for part of each cycle, after enough cycles, the stress relaxes to a measurably lower value. We then track the evolution of these jammed states by considering g^2 for the most compressed states. The corresponding time series of g^2/g_0^2, for several packing fractions of ellipses and disks (the most compressed ϕ is used as a label here), are shown in Fig. 3(a). Here, we emphasize the relaxation that occurs for states with the most compressed packing fractions that are above the isotropic jamming point. However, there is a largest ϕ_m such that we do not see significant particle or stress relaxation over ~1000 cycles. For instance, the time series of disks corresponding to $\phi = 0.868$ in Fig. 3(a) pertains to a packing fraction that is lower than ϕ_m^{disks}, even though the fully compressed density for these data is above the isotropic jamming density of $\phi \simeq 0.84$. At a higher

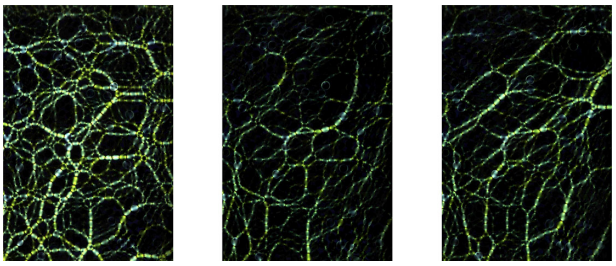

FIG. 2 (color online). Photoelastic images showing how the force network evolves over 999 cycles of cyclic compression, applied to a system of disks at $\phi = 0.863$. The cycle numbers of images from left to right are 1, 500, and 999.

packing fraction (i.e., $\phi = 0.883$), the global g^2 is persistent for many cycles, in the sense that there is no overall change in the peak g^2 with cycle number. We conclude that there is a range of ϕ for which the very small amount of spatial freedom, coupled with the compressive or dilational driving, is sufficient to allow structural rearrangement.

In Fig. 2, we show photoelastic images of disks for the maximum compressions of cycles 1, 500, and 999. Note that the stress network of the most compressed states changes spatially, while the overall stress relaxes over cycle number.

In order to quantify the long-term stress relaxation as in Fig. 3(a), we fit the time series to the functional form

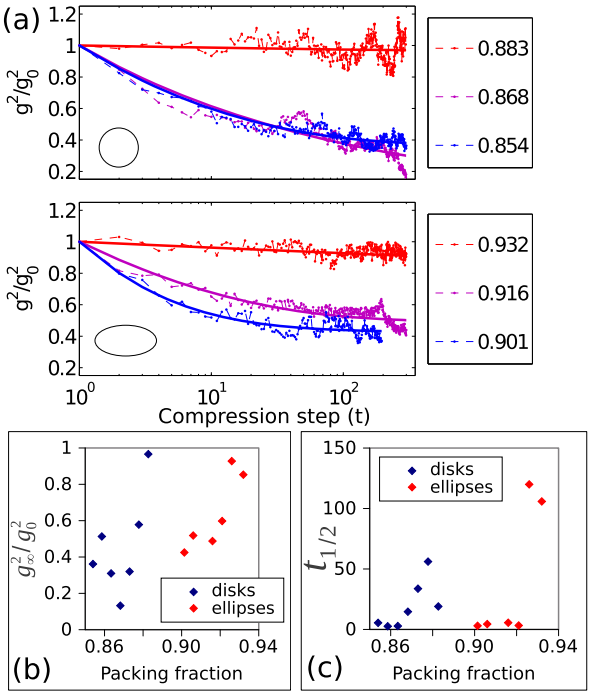

FIG. 3 (color online). (a) Time series of global g^2 for representative systems of disks and ellipses under maximum compression. Colors represent packing fractions at the most compressed state of each cycle. (b) Data for g_∞^2, determined from a fit to $g^2/g_0^2 = [t + t_0/t(t_0 + 1)]^a$. (c) Relaxation time for g^2/g_0^2 to relax halfway between its initial value of 1 and g_∞.

$g^2/g_0^2 = A[(t_0/t) + 1]^a$, which captures both the initial relatively fast drop and the long-time saturation to a final value, g_∞^2/g_0^2. Since we have one more constraint on parameters at $t = 1$, i.e., $A(t_0 + 1)^a = 1$, the functional form reduces to $g^2/g_0^2 = [t + t_0/t(t_0 + 1)]^a$. The fitted curves are shown by solid lines in Fig. 3(a). The large time value is $g_\infty^2/g_0^2 = (1 + t_0)^{-a}$, and it is straightforward to compute the time $t_{1/2}$ for g^2/g_0^2 to fall from 1.0 to $(1 + g_\infty^2/g_0^2)/2$.

From the parameters a and t_0, obtained from the least-squares fits, we find g_∞^2/g_0^2 and $t_{1/2}$ as a function of density for both disks and ellipses, which we then show in Figs. 3(b) and 3(c). Although there is a fair bit of scatter, the time scale $t_{1/2}$ grows strongly and g_∞^2/g_0^2 jumps quickly to 1.0, above a characteristic maximal packing fraction ϕ_m, where the system becomes effectively frozen; at least on the time of these experiments, there is little evolution of the global stress for either ellipses or disks for cyclic compression carried out above this density. From g_∞^2/g_0^2 values, we estimate $\phi_m \simeq 0.88$ for disks and $\phi_m \simeq 0.93$ for ellipses. For densities above ϕ_m, the system maintains a global g^2 and a memory of its previous state for seemingly arbitrarily large numbers of compression cycles. To the best of our knowledge, this work is the first observation of such an effect.

Particle motion vs stress evolution.—Given that the present systems can compact over long time scales, an interesting question is whether the dynamical process of gradual compaction is associated with identifiable, and possibly heterogeneous, structural changes (i.e., in the particle positions). In order to probe the effect of particle motion, we first consider the mobility of particles, defined as the displacement of the particle for a given time delay τ, relative to the mean displacement of all particles. (Here, time represents the number of compression cycles.) Figure 4 shows data for two different time delays, $\tau = 10$ and $\tau = 1000$, in a compression experiment on ellipses. Particles with similar mobility are represented by similar colors in Fig. 4. Specifically, the colors correspond to the

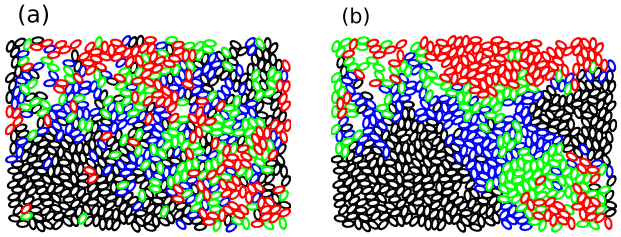

FIG. 4 (color online). Mobility of the particles (ellipses) in an arbitrary time. The packing fraction of the system is $\phi = 0.932$. The time delay τ equals (a) 10 cycles and (b) 1000 cycles. The various colors represent particles with a similar mobility range. Specifically, the colors correspond to the following fractional changes relative to all the particles: red, 0.90 ± 0.1; green, 0.70 ± 0.10; blue, 0.50 ± 0.10; and black, 0.20 ± 0.20.

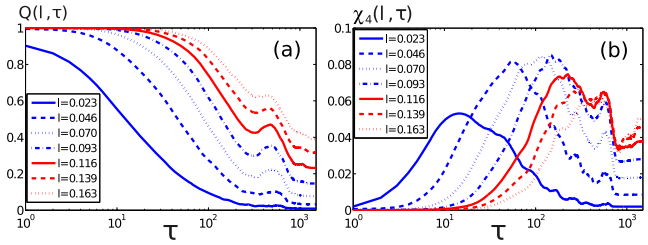

FIG. 5 (color online). (a) $Q_s(\tau)$ and (b) $\chi_4(\tau)$ for a system of isotropically compressed ellipses with a (highest) packing fraction of $\phi = 0.916$. The unit of length scale, l, is the semiminor axis of an ellipse.

following fractional changes relative to all the particles: red, 0.90 ± 0.1; green, 0.70 ± 0.10; blue, 0.50 ± 0.10; and black, 0.20 ± 0.20. Although the spatial distribution of most mobile particles changes substantially over time, the regions of comparable mobility form very large clusters. This indicates heterogeneous dynamics both in time and space. The dense structure of these clusters suggests that there are, at best, small local rearrangements of the particles.

As an alternative approach to quantifying this heterogeneous dynamics, we have studied the four-point susceptibility $\chi_4(\tau)$, which indicates the extent of temporal correlation of dynamics at any pair of spatial points [3]. Here, $\chi_4(\tau)$ is defined as $\chi_4(\tau) = N[\langle Q_s(\tau)^2\rangle - \langle Q_s(\tau)\rangle^2]$. We choose $Q_s(t) = (1/N)\sum_{i=1}^{N} w(|r_i(t) - r_i(0)|)$, with

$$w = \begin{cases} 1 & \text{if } |r_i(t) - r_i(0)| < l, \\ 0 & \text{otherwise.} \end{cases}$$

N is the number of particles, and $r_i(t)$ indicates the particle positions at time t, for a length scale l. The averages are taken over all the particles and over all starting times. $Q_s(\tau)$, which is referred to as the self-overlap order parameter, is a measure of particle mobility and is quantified by a length scale l [3]. We plot $Q_s(\tau)$ and $\chi_4(\tau)$ vs l in Fig. 5. As seen, Q_s varies from 1 to 0 as the time delay τ increases. On the other hand, χ_4 has a maximal point for each l, which basically characterizes a time delay τ^*, by which the particles, on average, move more than the length scale l.

As seen in Fig. 5(b), χ_4 is maximal for the characteristic length scale $l^\dagger \simeq 0.093$. We now take the characteristic $l^\dagger$ for each packing fraction and find the corresponding maximal $\tau^\dagger$. The data are demonstrated in Fig. 6. We note that a similar structure for χ_4 has been obtained under much more energetic driving conditions by Dauchot and coworkers [4]. There are several remarkable features in these data. First, the typical length scales for l are only a fraction of a particle diameter; the particles are largely confined. Second, the characteristic times $\tau^\dagger$ are relatively insensitive to ϕ but are an order of magnitude greater for ellipses than for disks.

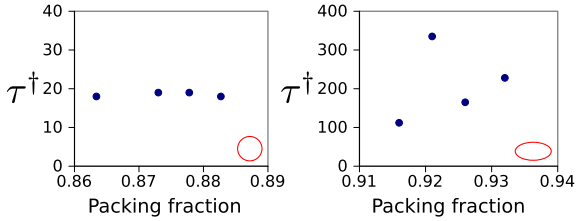

FIG. 6 (color online). $\tau^\dagger$ vs packing fraction ϕ for systems of ellipses and disks. As seen, the average value of $\tau^\dagger$ is about an order of magnitude larger for ellipses compared to disks.

These results beg the question, where should one look to observe the stress relaxation demonstrated in Fig. 3(a). In fact, the distribution of forces demonstrated by photoelastic response in Fig. 2 shows that although the particles may move very little, even a tiny bit of freedom allows the force network to evolve and relax substantially in time.

Conclusions.—We have observed transient stress states that occur for both systems of disks and ellipses that are cyclically compressed by a modest amount above the isotropic jamming point (point J). The global stress relaxes to a stationary value in the course of many compression cycles. The time corresponding to stress relaxation grows substantially above a characteristic packing fraction ϕ_m (ellipses: $\phi_m = 0.93$; disks: $\phi_m = 0.88$). We have sought to identify the origin of the stress relaxation. To do so, we first characterized the structural changes by computing relative mobilities and χ_4. In particular, the characteristic time scale $\tau^\dagger$ varied rather little with ϕ, whereas the stress relaxation showed a significant change by increasing ϕ. However, the analysis of χ_4 did identify significantly longer times for $\tau^\dagger$ in the case of ellipses, which we attribute to the fact that ellipses are substantially confined by their inability to rotate. In fact, the most clearly identifiable relaxation occurs in the force network, even though there is minimal particle motion. An interesting issue for future work concerns the extent to which interparticle friction plays a role in the relaxation process. For disks, friction may be more important in stabilizing packings than for ellipses, where rotational constraints do occur even without friction.

This work is supported by NSF Grant No. DMR-1206351, NASA Grant No. NNX10AU01G, and ARO Grant No. W911-NF-1-11-0110.

[1] L. Berthier, G. Biroli, J. Bouchaud, L. Cipelletti, and W. van Saarloos, *Dynamical Heterogeneities in Glasses, Colloids, and Granular Media* (Oxford University Press, New York, 2011).
[2] N. Lačević and S. C. Glotzer, J. Phys. Chem. B **108**, 19623 (2004).
[3] A. S. Keys, A. R. Abate, S. Glotzer, and D. Durian, Nat. Phys. **3**, 260 (2007).

[4] O. Dauchot, G. Marty, and G. Biroli, Phys. Rev. Lett. **95**, 265701 (2005).
[5] S. Glotzer, J. Non-Cryst. Solids **274**, 342 (2000).
[6] C. Coulais, R. P. Behringer, and O. Dauchot, Europhys. Lett. **100**, 44005 (2012).
[7] P. Richard, M. Nicodemi, R. Delannay, P. Ribière, and D. Bideau, Nat. Mater. **4**, 121 (2005).
[8] P. Philippe and D. Bideau, Europhys. Lett. **60**, 677 (2002).
[9] F. Lechenault, O. Dauchot, G. Biroli, and J. P. Bouchaud, Europhys. Lett. **83**, 46003 (2008).
[10] F. Alonso-Marroquín and H. J. Herrmann, Phys. Rev. Lett. **92**, 054301 (2004).
[11] S. Farhadi and R. P. Behringer, Phys. Rev. Lett. **112**, 148301 (2014).
[12] D. Howell, R. P. Behringer, and C. Veje, Phys. Rev. Lett. **82**, 5241 (1999).
[13] J. H. Snoeijer, W. G. Ellenbroek, T. J. H. Vlugt, and M. van Hecke, Phys. Rev. Lett. **96**, 098001 (2006).
[14] J. Ren, J. A. Dijksman, and R. P. Behringer, Phys. Rev. Lett. **110**, 018302 (2013).
[15] H. M. Jaeger and S. R. Nagel, Science **255**, 1523 (1992).
[16] H. M. Jaeger, S. R. Nagel, and R. P. Behringer, Rev. Mod. Phys. **68**, 1259 (1996).
[17] T. S. Majmudar and R. P. Behringer, Nature (London) **435**, 1079 (2005).
[18] T. S. Majmudar, M. Sperl, S. Luding, and R. P. Behringer, Phys. Rev. Lett. **98**, 058001 (2007).
[19] S. Farhadi, Ph.D. Thesis, Duke University, 2012.